Supplementary Information for:

Kinetically Stabilized Perovskites via Selective Iodoplumbate Cold Casting for High-Efficiency Bilayer 3D:2D Photovoltaic Module

Authors: Yeoun-Woo Jang[1,2], Seungmin Lee[3], Yongseok Yoo[4,5], Isaac Metcalf[6], Hee Jeong Park[5,7], Byeongjun Gil[8,9], Jihun Jang[10], Jared Fletcher[11], Faiz Mandani[1], Jianlin Zhou[1], Seunghwan Bae[5], Miyoung Kim[8], Jun Hong Noh[3,12], Mercouri G. Kanatzidis[11], Jacky Even[13], Mansoo Choi[2,14*] and Aditya D. Mohite[1*]

Affiliations:

[1]Department of Chemical and Biomolecular Engineering, Rice University, Houston, TX 77005, USA

[2]Global Frontier Center for Multiscale Energy Systems, Seoul National University; Gwanak-gu, Seoul 08826, Republic of Korea

[3]Green and Sustainable Materials R&D Department, Korea Institute of Industrial Technology (KITECH), Cheonan 31056, Republic of Korea

[4]School of Chemical and Biological Engineering, Seoul National University, Seoul 08826, Republic of Korea

[5]School of Civil, Environmental and Architectural Engineering, Korea University, Seoul 02841, Republic of Korea

[6]Department of Materials Science and Nanoengineering, Rice University, Houston, TX 77005, USA

[7]Department of Chemical and Biological Engineering, Korea University, Seoul 02481, Republic of Korea

[8]Department of Materials Science and Engineering and Research Institute of Advanced Materials, Seoul National University, Seoul 08826, Korea

[9]Condensed Matter Physics and Materials Sciences Department, Brookhaven National Laboratory, Brookhaven, NY 11973, USA

[10]Frontier Energy Solution Co., Ltd., Ulsan 44412, Republic of Korea

[11]Department of Chemistry, Northwestern University, Evanston, IL 60208, USA

[12]Department of Integrative Energy Engineering & KU-KIST Green School Graduate School of Energy and Environment, Korea University, Seoul 02841, Republic of Korea

[13]Univ Rennes, INSA Rennes, CNRS, Institut FOTON (Fonctions Optiques pour les Technologies de l'Information), UMR 6082, Rennes, France

[14]Department of Mechanical Engineering, Seoul National University, Seoul 08826, Korea
*Corresponding author. Email: mchoi@snu.ac.kr (M. C.) and adm4@rice.edu (A.D.M.)

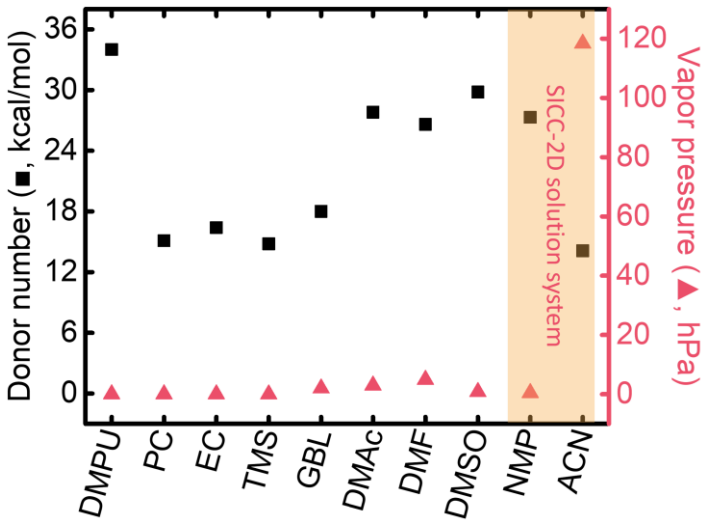

Supplementary Figure S1. Gutmann's donor number and vapor pressure of solvents. Gutmann's donor number is represented by black rectangles and vapor pressure is indicated by red triangles. The figure shows the results for DMPU (N,N′-Dimethylpropyleneurea), PC (Propylene carbonate), EC (Ethylene carbonate), TMS (Tetramethylene sulfone), GBL (γ-butyrolactone), DMAc (Dimethylacetamide), DMF(Dimethylformamide), DMSO (Dimethyl sulfoxide), NMP (N-Methyl-2-pyrrolidone) and ACN (Acetonitrile), and among them, ACN and NMP were selected, which are solutions that have very different properties and mix well with each other.

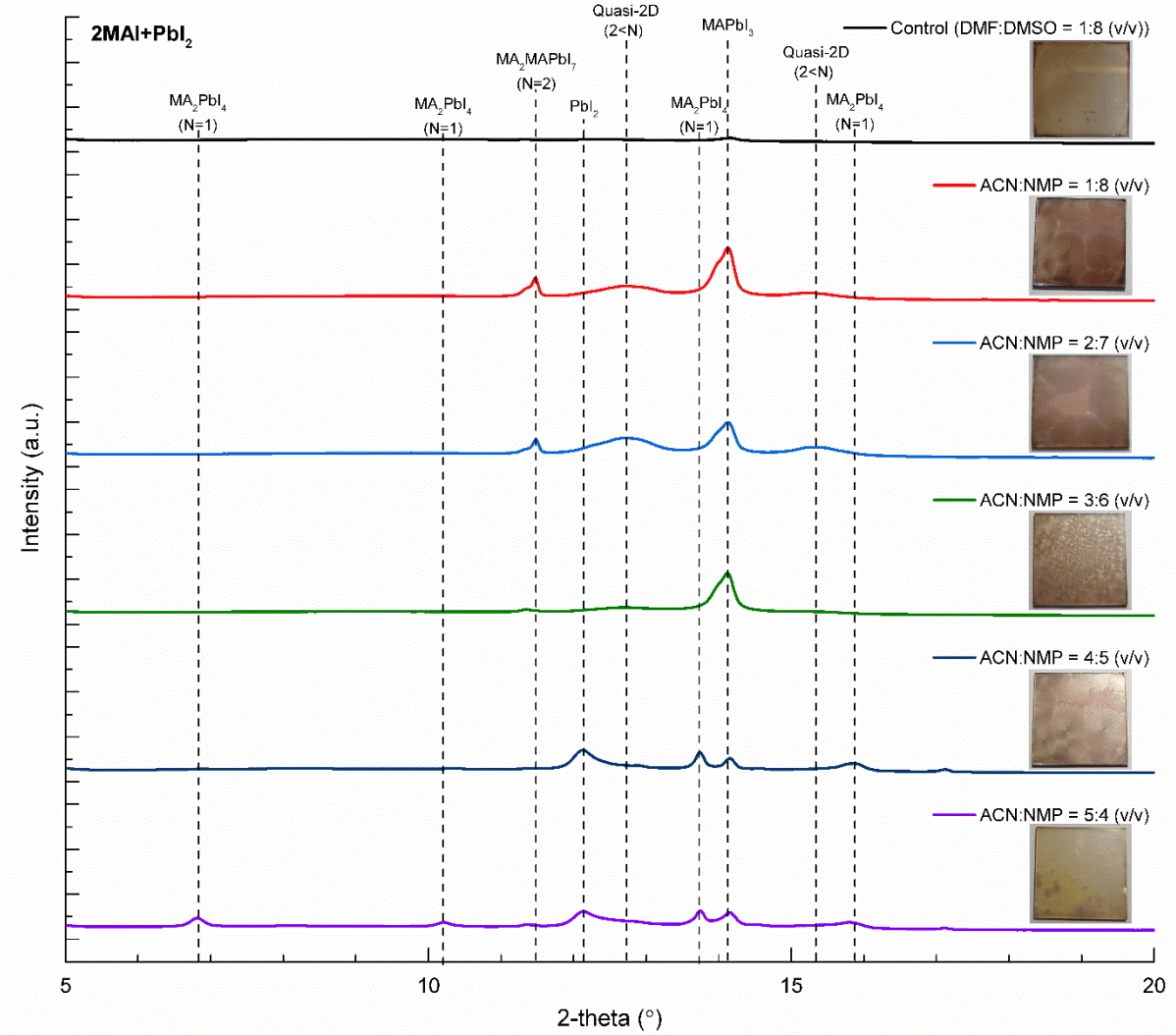

Supplementary Figure S2. X-ray diffraction curves of MA_2PbI_4 thin films prepared using precursor solutions with varying solvent compositions. Insets show photographs of the corresponding thin films obtained under each condition.

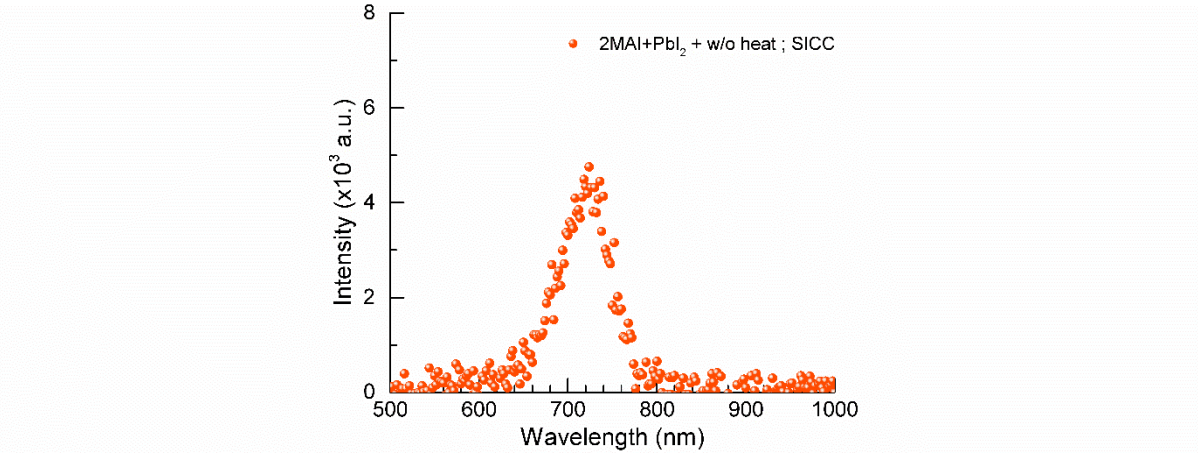

Supplementary Figure S3. Photoluminescence spectrum of MA_2PbI_4 perovskite fabricated from SICC process. The perovskite film was prepared by mixing MAI and PbI_2 in a 2:1 molar ratio without thermal heating. The substrate is ITO.

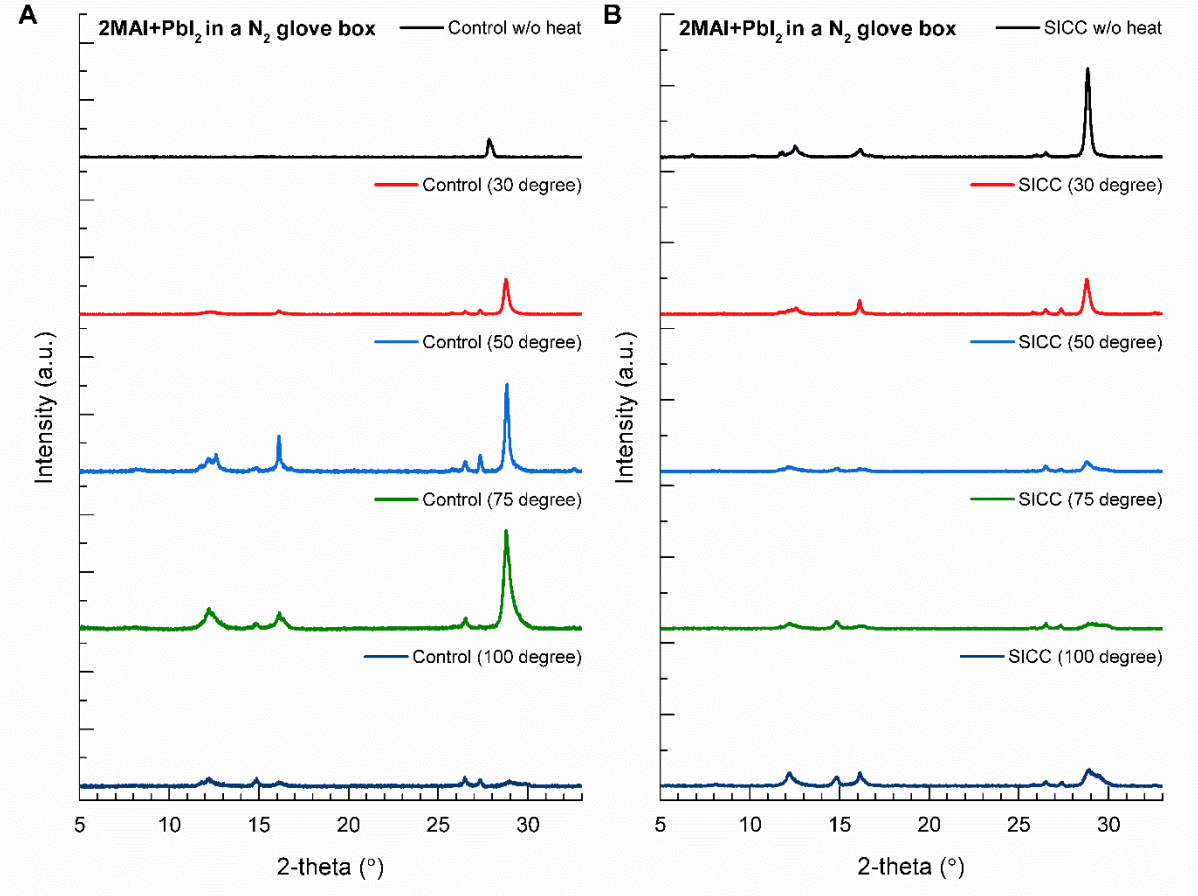

Supplementary Figure S4. X-ray diffraction (XRD) patterns showing the effect of annealing temperature on thin films prepared from MAI and PbI_2 (2:1 molar ratio) inside an N_2-filled glovebox. The patterns compare films fabricated via (A) a control process and (B) the SICC process.

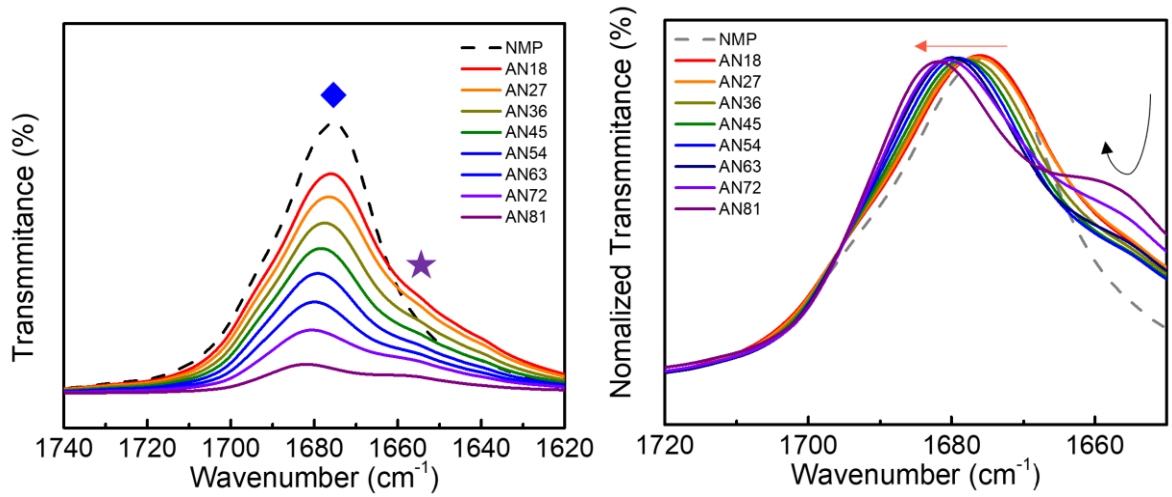

Supplementary Figure S5. Fourier-transform infrared spectroscopy (FTIR) results of BA_2PbI_4 solutions according to solvent composition ratio. AN#1#2 refers to a solution in which ACN (Acetonitrile) and NMP (N-Methyl-2-pyrrolidone) are mixed in a composition ratio of #1:#2, respectively. The blue diamond indicates the C=O double bond stretch in NMP and the purple star indicates the C-H bending in BA (butylamine). The graph on the left is the original absolute value graph, and the graph on the right is the normalization of each graph to the maximum value of the corresponding section.

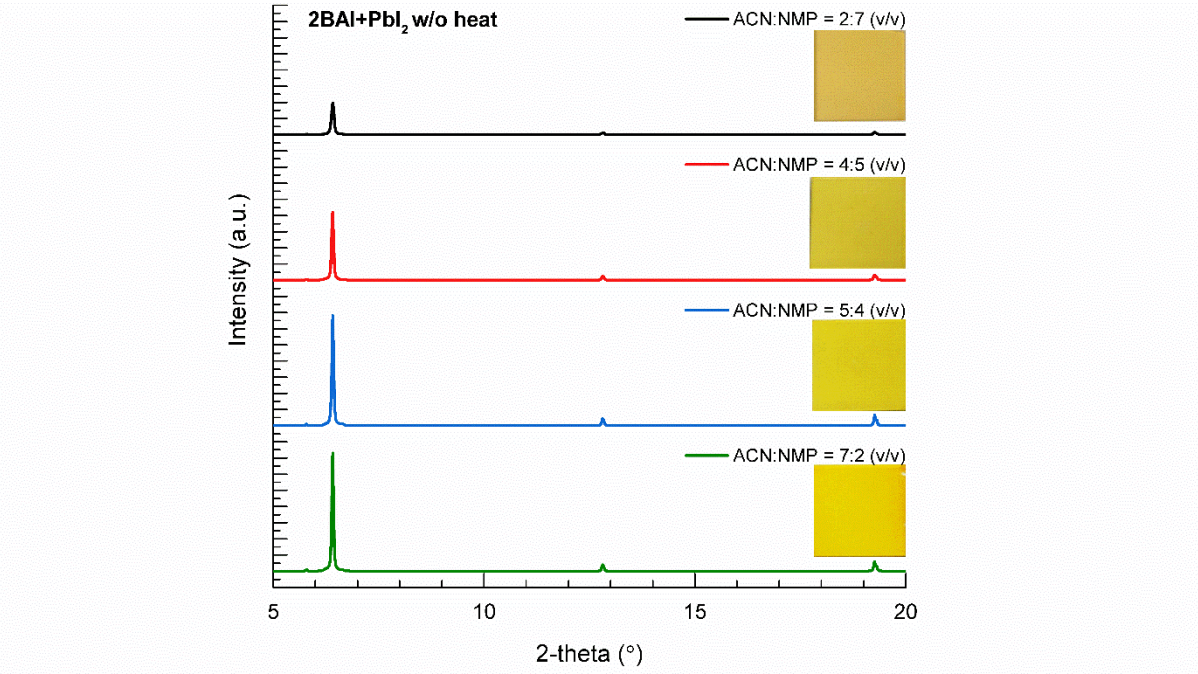

Supplementary Figure S6. X-ray diffraction patterns of BA_2PbI_4 2D perovskite films prepared using 0.25 M precursor solutions in mixed ACN and NMP solvents. The solvent volume ratio was varied as ACN:NMP = x:(9-x), where x = 2, 4, 5, and 7. Insets show photographs of the corresponding each condition.

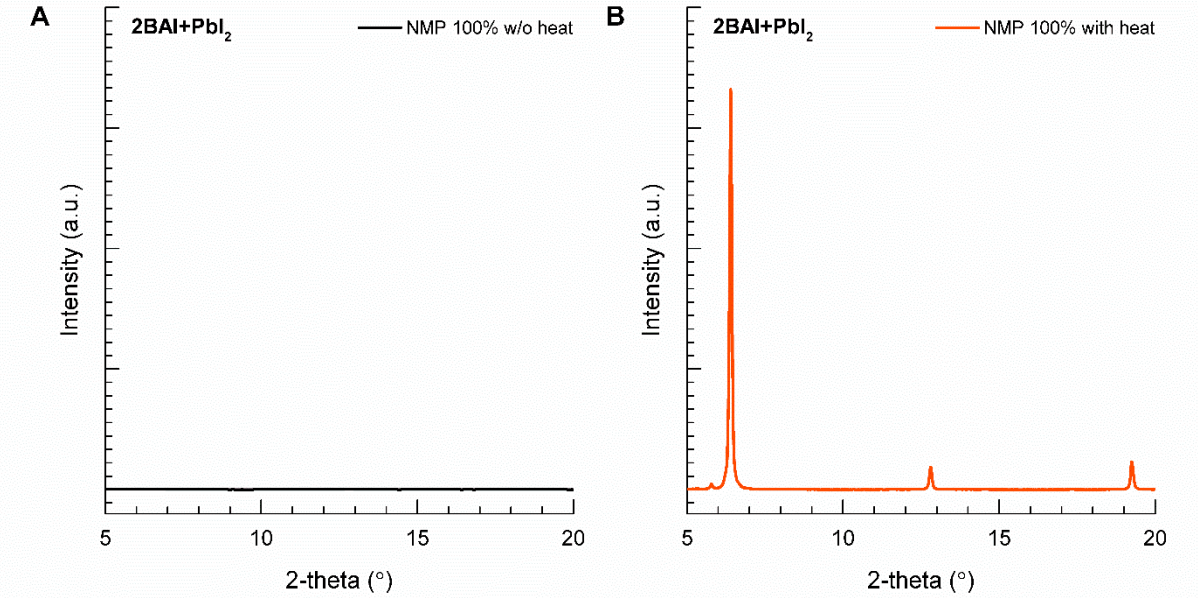

Supplementary Figure S7. X-ray diffraction patterns of thin films prepared from BAI:PbI_2 (2:1 molar ratio) in NMP. (A) As-deposited film, spin-coated without thermal annealing. (B) Film after spin-coating and subsequent annealing at 100°C for 5min.

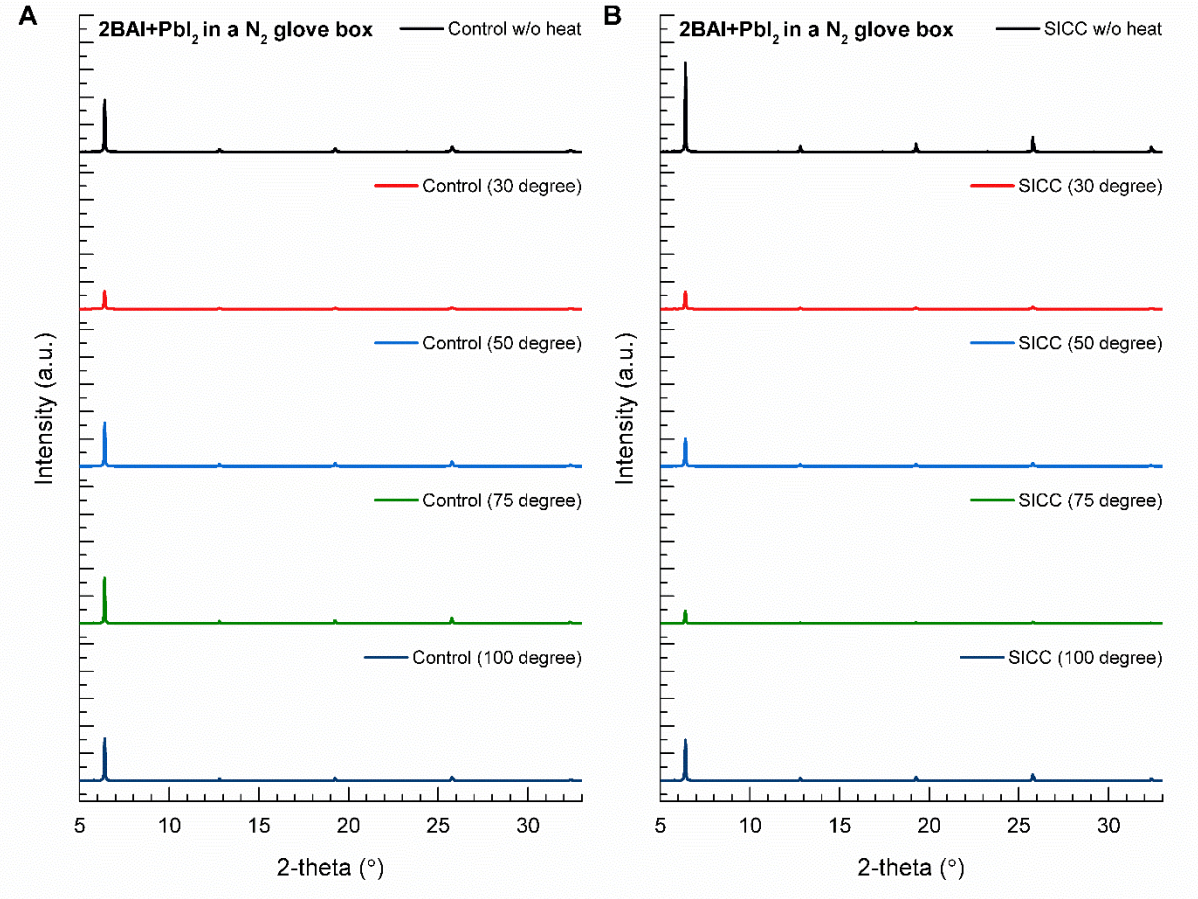

Supplementary Figure S8. X-ray diffraction (XRD) patterns showing the effect of annealing temperature on thin films prepared from BAI and PbI_2 (2:1 molar ratio) inside an N_2-filled glovebox. The patterns compare films fabricated via (A) a control process and (B) the SICC process.

Supplementary Table 1. Bragg reflection positions and FWHM (Full Width at Half Maximum) of (00l) peaks before and after heating of Control and SICC films formed on ITO glass. In the case of the control, the FWHM values of the (006), (008), and (0010) diffraction peaks were obtained from curve fitting results.

Plane	Control w/o heat		Control with heat		SICC w/o heat		SICC with heat	
	Peak (°)	FWHM (°)	Peak (°)	FWHM (°)	Peak (°)	FWHM (°)	Peak (°)	FWHM (°)
(002)	6.41	0.088	6.42	0.112	6.41	0.082	6.42	0.112
(004)	12.81	0.097	12.85	0.125	12.82	0.095	12.85	0.127
(006)	19.26	0.110	19.32	0.145	19.27	0.110	19.32	0.146
(008)	25.77	0.129	25.86	0.171	25.86	0.170	25.86	0.170
(0010)	32.67	0.152	32.49	0.202	32.40	0.159	32.49	0.202

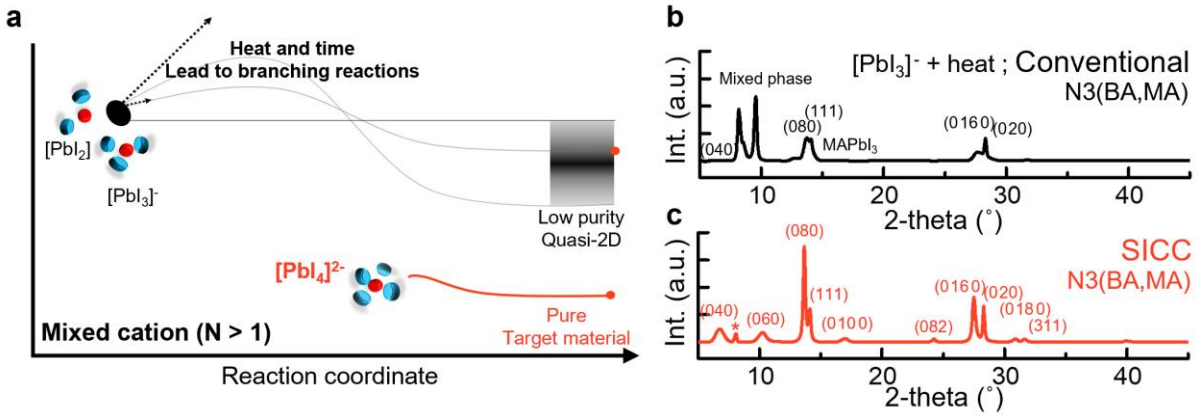

Supplementary Figure S9. Problems with thin films produced through conventional methods. a, Applying heat and time to an uncontrolled precursor promotes the growth of a compact structure and facilitates more diverse branching reactions when the solution includes 3D favorable cation. **b,** the XRD results of the conventional method are observed with various N phases, and even include some 3D perovskite. **c,** a result of the optimized SICC process, only the target material is formed and all ideal picks are observed.

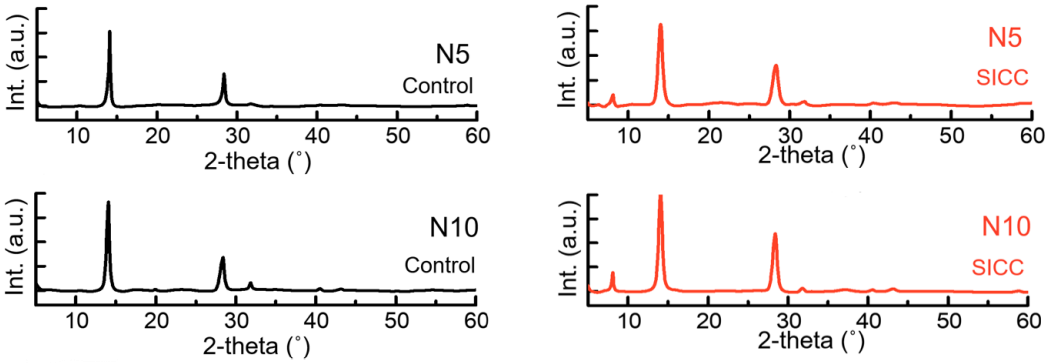

Supplementary Figure S10. 1D-XRD results for higher n values 2D perovskites

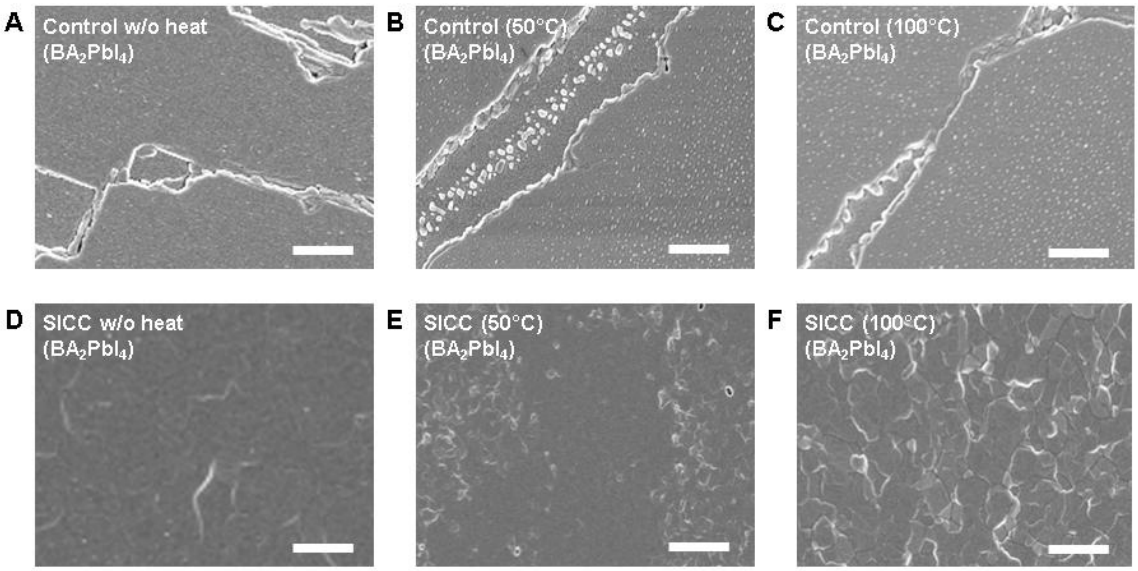

Supplementary Figure S11: Top-view scanning electron microscopy (SEM) images compare BA_2PbI_4 perovskite films prepared via a control process, showing (A) the as-prepared film (no annealing), (B) the film annealed at 50°C, and (C) the film annealed at 100°C, alongside films prepared via the SICC process, showing (D) the as-prepared film (no annealing), (E) the film annealed at 50°C, and (F) the film annealed at 100°C. The annealing time was 5 min for all heat-treated conditions. All scale bars represent 1μm.

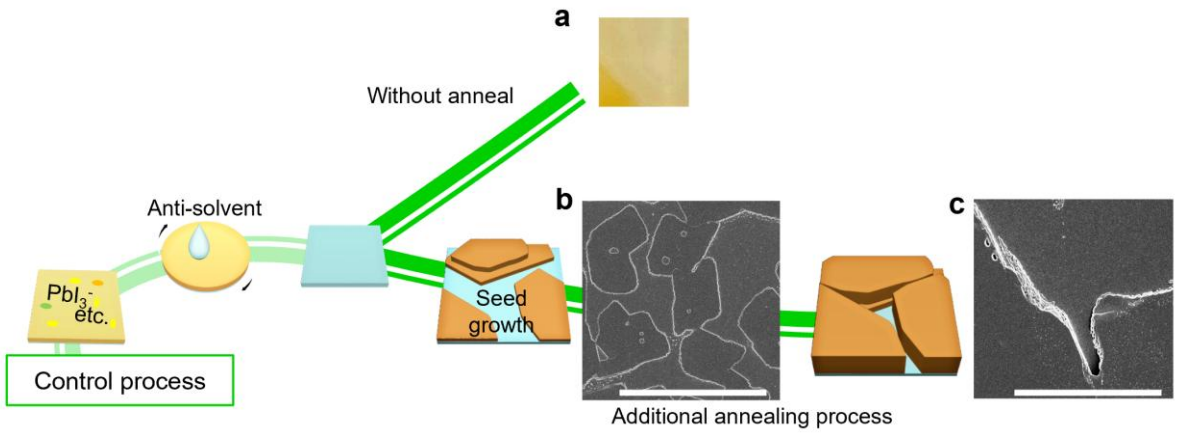

Supplementary Figure S12. Schematic of the crystallization reaction for the control process. In the control process, a mixed solution of DMF and DMSO at a volume ratio of 8:1 is used and heated to 100 degrees for 10 minutes. **a,** When using the same solution as the control but without heating, a film with non-uniform surface states is produced. **b and c,** In the control reaction, (b) square-shaped island-like seed growth occurs, (c) with grain sizes growing to several micrometers or more. However, even after final growth, cracks of about 1 μm in size are present. The scale bars in all SEM (Scanning electron microscope) image indicate 1 μm.

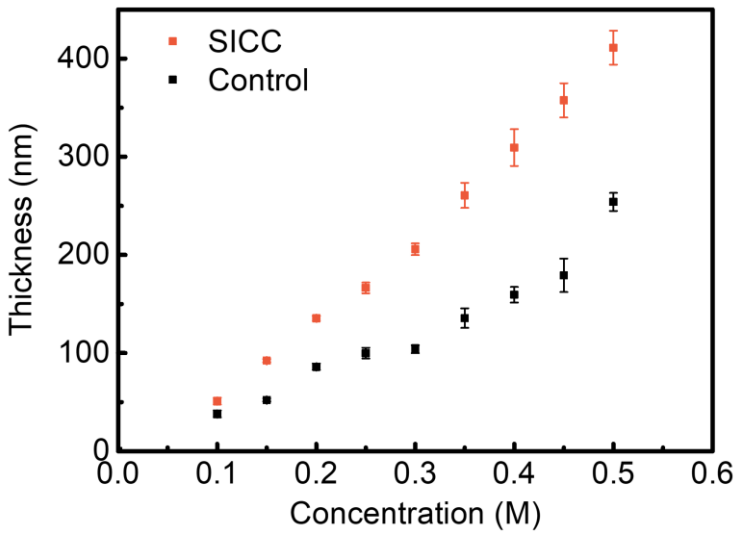

Supplementary Figure S13. The correlation between concentration of solution and thickness of 2D perovskite thin films. Each value represents the average of multiple spots within one sample, and the error bar indicates the difference in average values between different samples. Optical measurements and stability measurements were conducted using similar thicknesses for consistency.

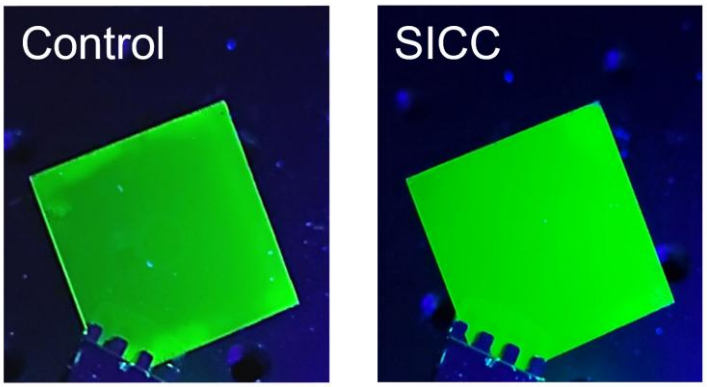

Supplementary Figure S14. 365 nm lamp radiated the BA_2PbI_4 film in dark.

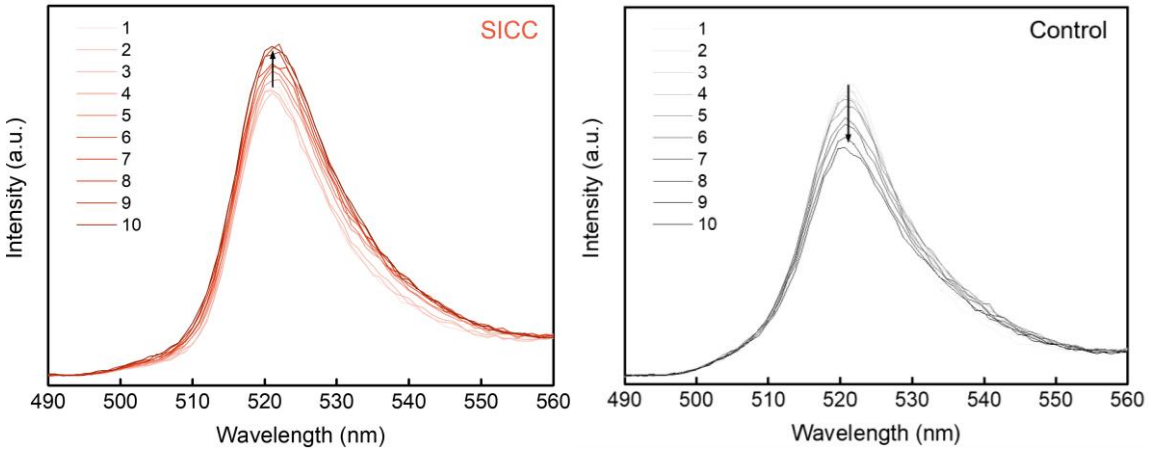

Supplementary Figure S15. The repeated steady state photoluminescence (steady state PL) measurement results. The measurements were repeated at 3-minute intervals using a laser with a power density of 73.7 mW/cm^2. Photon flux is $1.80 \cdot 10^{17}$/cm^2

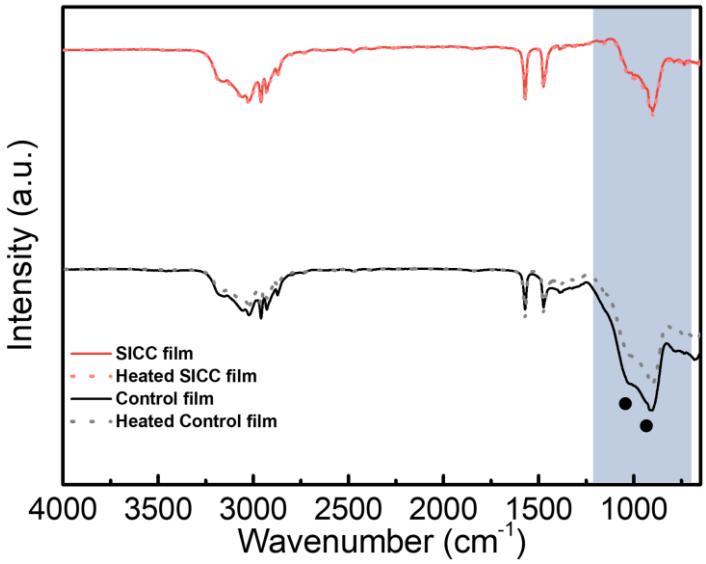

Supplementary Figure S16. FTIR results of BA_2PbI_4 films. The red lines represent the SICC sample, and the black lines represent the control sample. Solid lines represent data from samples without heating, while dashed lines represent data from samples heated at 100 degrees for 30 minutes. The heating leads to a gradual decrease in the signal mostly from the area marked by black circles in the control sample (presumed to be DMSO; S=O stretching; 1320-1030, 730 cm^{-1}). In contrast, there is no additional change observed due to heat in the SICC sample.

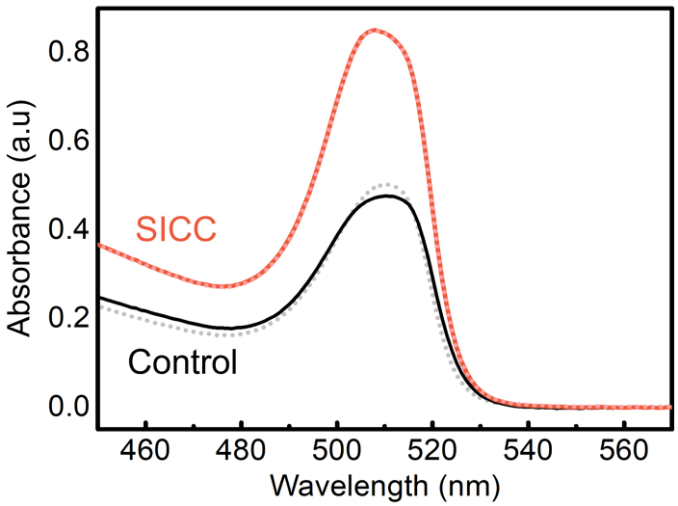

Supplementary Figure S17. Absorbance spectra of BA_2PbI_4 films. The red lines represent the SICC sample, and the black lines represent the control sample. Dashed lines represent data from samples without heating, while solid lines represent data from samples heated at 100 degrees for 30 minutes additionally. Each sample was fabricated with a similar thickness. In the specific absorption range, the SICC sample shows better absorption and thermal stability, whereas the control sample undergoes changes.

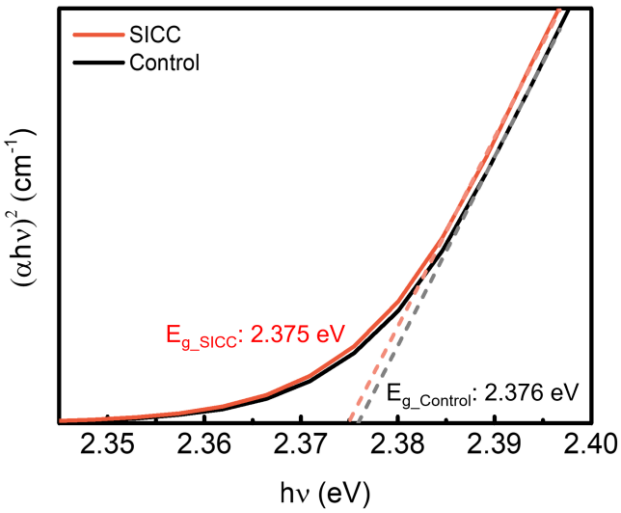

Supplementary Figure S18. Tauc plot for BA_2PbI_4 dependent on each process. The optical bandgaps (E_g) were indicated 2.375 eV (SICC) and 2.376 eV (control), respectively.

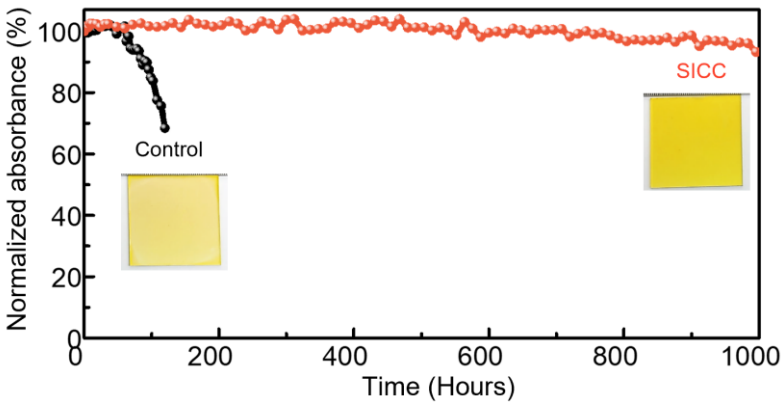

Supplementary Figure S19. The results of humidity test under 70% relative humidity (RH) at room temperature. While maintaining a humidity of 70%, the device was exposed to indoor light through the glass window. Neither of the two BA_2PbI_4 samples was encapsulated. Each inset image was captured between 100 hours and 1000 hours after completing each measurement. The measurements targeted the center of the film, and after 100 hours, the initial absorbance of the control sample dropped to below 70%, while the SICC sample maintained a level of over 92% after 1000 hours.

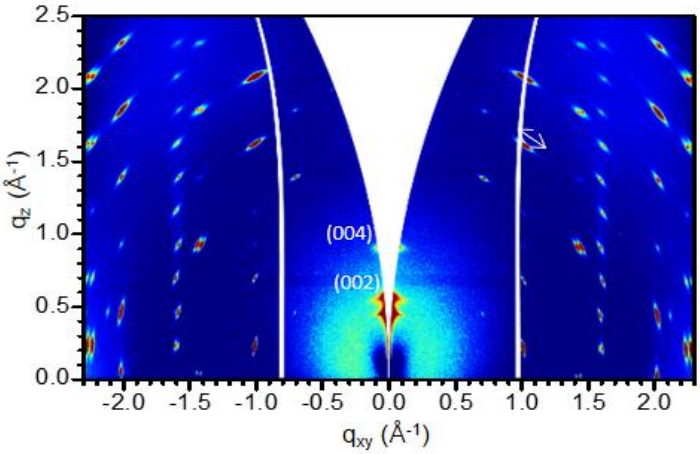

Supplementary Figure S20. GIWAXS patterns of the 250nm thick BA_2PbI_4 film fabricated by control process. The incident angle is 0.254 º.

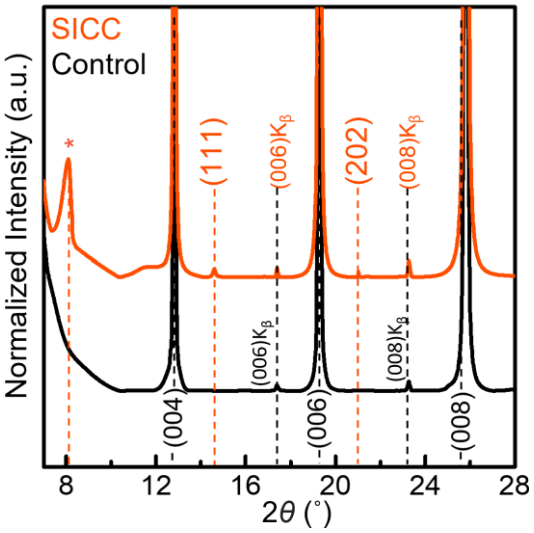

Supplementary Figure S21. The High resolution 1D X-ray diffraction (HR 1D-XRD) patterns of BA_2PbI_4 films. The asterisk indicates 8.08 º.

Supplementary Table 2. Full Width at Half Maximum (FWHM) of the (00l) with l=2n Bragg reflections. The films are formed on ITO glass via spin coating. In the case of the control, the FWHM values of the (006), (008), and (0010) peaks are obtained from the curve fitting results.

Plane	SICC		Control	
	Peak (º)	FWHM (º)	Peak (º)	FWHM (º)
(002)	6.40	0.16	6.39	0.19
(004)	12.82	0.17	12.81	0.20
(006)	19.28	0.18	19.26	0.25
(008)	25.81	0.19	25.80	0.24
(0010)	32.42	0.21	32.41	0.28

Supplementary Note 1. Calculation of the correlation length within the film in both vertical and horizontal directions using the Halder-Wagner (H-W) plot.

Line profile analysis of X-ray diffraction serves as a tool for quantifying microstructural characteristics of crystals, such as crystalline size, correlation lengths, and micro-strains. Typically, this analysis relies on the use of Lorentzian and Gaussian functions to characterize diffraction peaks. However, these functions often fail to perfectly match the observed peaks. To address this issue, the Halder-Wagner method[28] incorporates Voigt functions[36,37], which better account for the peak shape. The Voigt function is a convolution of Lorentzian and Gaussian functions. Thus, in the Halder-Wagner approach, the parameter $\beta\,(s)$, representing the integrated breadth (IB) or full width at half maximum (FWHM) of the Voigt function, is expressed as shown in Equation 1.

$$\beta^2(s) = \beta_{Lorentz}(S) \cdot \beta(s) + {\beta_{Gauss}}^2(S) \qquad \text{[Equation 1]}$$

Here, $\beta_{Lorentz}(S)$ and $\beta_{Gauss}(S)$ represent FWHM obtained from Lorentzian and Gaussian functions, respectively. The Halder-Wagner method assigns greater significance to peaks occurring at lower and intermediate diffraction angles, aiming to reduce the overlap between diffraction peaks. The relationship between the correlation length (L) and micro-strain (ε) can be described by Equation 2.

$$\left(\frac{\beta\,(s)}{S}\right)^2 = 4\varepsilon^2 + \frac{0.9}{L}\frac{\beta(s)}{S^2} \qquad \text{[Equation 2]}$$

Where, the variable S is defined as $S = \frac{2\sin\theta}{\lambda}$, and $\beta\,(s)$ represents the IB, which can be expressed as $\beta(s) = \beta(\theta)\frac{\cos\theta}{\lambda}$ or FWHM. Specifically, in this study, it was observed that linear plotting using FWHM of the Voigt function for β(s) provided a better fit compared to using the full width. Therefore, it is reasonable to utilize the FWHM of the Voigt function for $\beta\,(s)$.

Initially, the correlation length along the Z-axis (vertical direction) was determined by employing as $\beta\,(s)$ the FWHM values obtained from the Voigt function for all (00l) Bragg reflections with l=2n identified in the XRD pattern. Subsequently, the correlation length for the X-axis was computed using Equation 2 with the peaks from longitudinal cut in the GIWAXS. Here, L represents the defect-free, denoting the correlation length (L). The outcomes are outlined in Supplementary Tables 2 and 3, presenting the values of L for the Z-axis direction and the X-axis direction, respectively.

Supplementary Table 3. The correlation length and calculation parameters in the z-axis direction (vertical).

Plane	SICC			Control		
	$\beta(s)/S^2$	$(\beta(s)/S)^2$	L (nm)	$\beta(s)/S^2$	$(\beta(s)/S)^2$	L (nm)
(002)	0.034	0.00062		0.041	0.00087	
(004)	0.009	0.00017		0.011	0.00024	
(006)	0.004	7.92E-05	55.80	0.005	0.00014	48.15
(008)	0.003	5.47E-05		0.003	8.79E-05	
(0010)	0.002	4.01E-05		0.003	8.52E-05	

Supplementary Table 4. The correlation length and calculation parameters in the x-axis direction (horizontal).

Plane	SICC			Control		
	$\beta(s)/S^2$	$(\beta(s)/S)^2$	L (nm)	$\beta(s)/S^2$	$(\beta(s)/S)^2$	L (nm)
(220)	0.003	7.90E-05	56.85	0.003	8.27E-05	40.70
(210)	0.004	0.00012		0.005	0.00015	
(020)	0.004	9.63E-05		0.005	0.00012	
(200)	0.005	0.00011		0.005	0.00014	

Supplementary Table 5. The angle between the plane within the bulk 2D perovskite film and the substrate.

Plane	D-spacing	cosθ	Angle with substrate
(002)	13.81	1.00	0.00 º
(202)	4.23	0.31	72.18 º
(111)	6.06	0.22	77.33 º

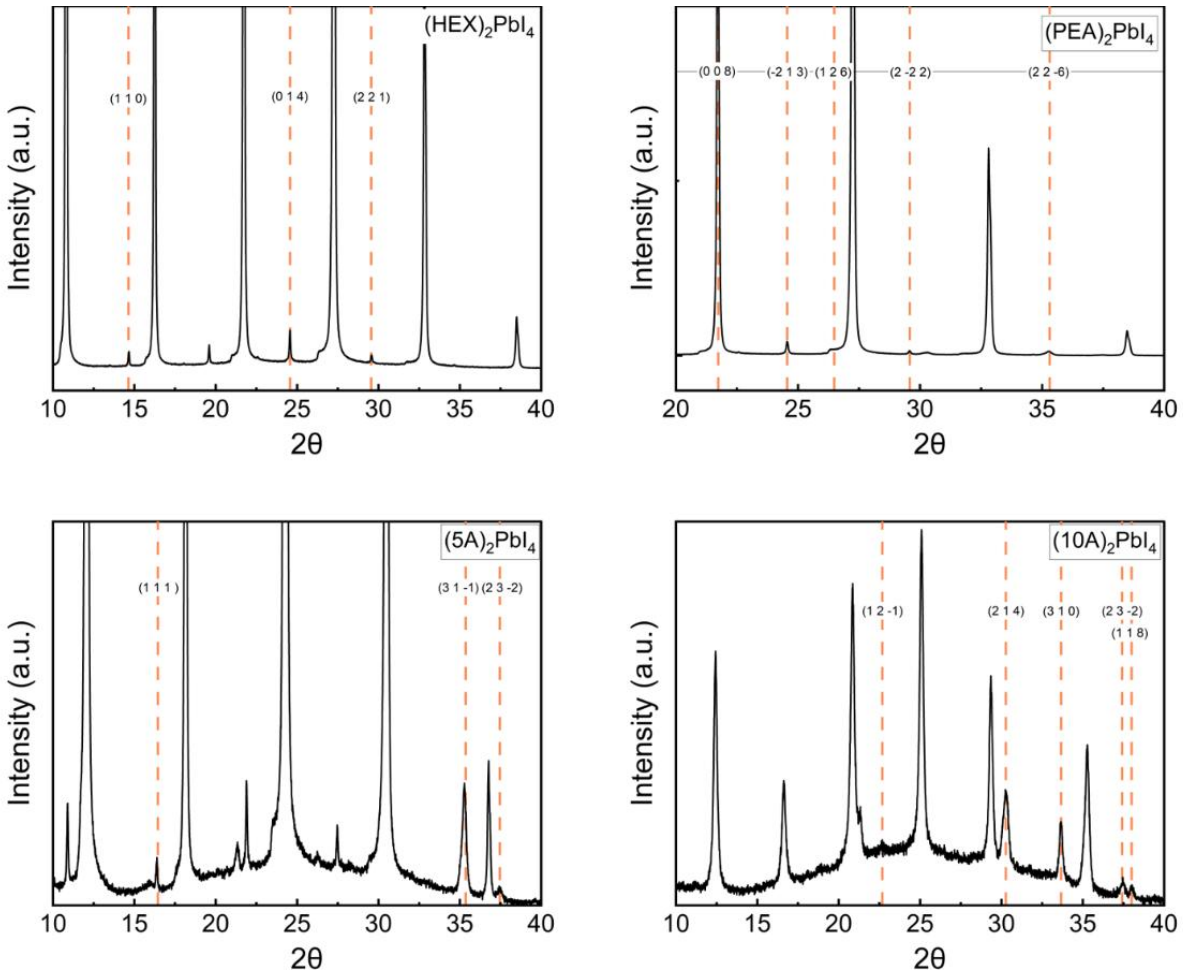

Supplementary Figure S22. 1D-XRD results of SICC 2D perovskite films fabricated using various 2D materials. The XRD results for SICC thin films made from various synthesized 2D perovskites are presented. The abbreviations for the cations are as follows: HEX = Hexylammonium, PEA = Phenethylammonium, 5A = Pentylammonium, and 10A = Decylammonium.

Supplementary Note 2. Crystallite Orientation Analysis using 4D-STEM

2.1 Orientation Mapping of SICC BA2PbI4 via Dimensionality Reduction

Diffraction patterns in transmission electron microscopy (TEM) depend on both crystal structure and crystallographic orientation. Crystal orientation is determined by analyzing the positions of diffraction peaks and the asymmetry in their intensity distributions. Four-dimensional scanning TEM (4D-STEM) facilitates the acquisition of 2D diffraction patterns arranged as a 2D array in real space, enabling the mapping of local orientation distributions within the specimen. The widely used methods, such as automated crystal orientation mapping (ACOM)[38], visualize in-plane or out-of-plane orientations through template matching of diffraction patterns. While these techniques accurately detect tilt components of orientation, they require distinct diffraction features, which are challenging to obtain when multiple crystallites align along the imaging direction.

Due to the small grain sizes of SICC BA2PbI4, which cause overlapping diffraction patterns, we opted for dimensionality reduction using non-negative matrix factorization (NMF) to identify primary diffraction components instead of relying on automated orientation mapping. **Supplementary Figure S23** illustrates the NMF decomposition, presenting 8 diffraction components alongside their corresponding real-space feature maps. These components were grouped into four sets based on pattern similarities: **Set 1**: Component 1 (background), **Set 2**: Components 2 and 4 (zone axis [001], red in Figure 3E), **Set 3**: Components 3 and 7 (zone axis [010], green in Figure 3E), **Set 4**: Components 5, 6, and 8 (other orientations, blue in Figure 3E). By assigning designated colors to the feature maps of each set and combining them, we constructed the orientation map shown in Figure 3E. While this map does not resolve subtle local orientation variations, it highlights the presence of distinct orientations, notably the [001] and [010] zone axes.

The blue regions of set 4, which do not align with the primary orientation sets, include additional orientations such as the (101) and (111) plane normal directions, as confirmed by XRD measurements. **Supplementary Figure S24** displays the virtual bright-field (v-BF) image corresponding to the orientation map in Figure 3E. Diffraction patterns from regions of interest (ROIs) 1 and 2, accompanied by simulated patterns and atomic models, indicate orientations close to the (101) and (111) plane normal directions, respectively, as detailed in Section 2.2 below.

2. 2. Determination of plane normal orientation in terms of lattice vector basis

Crystallographic orientations are typically expressed using real space vectors, which correspond to the unit cell parameters. This can lead to confusion when representing crystal plane directions, described by reciprocal vectors. In cubic systems, real and reciprocal vectors align, so the direction [u v w] matches the plane normal (u v w). Consequently, a diffraction pattern along the zone axis [u v w] indicates that the (u v w) plane is perpendicular to the electron beam's optic axis. In non-cubic systems, however, [u v w] does not necessarily correspond to (u v w), meaning the zone axis [u v w] does not ensure that the (u v w) plane is perpendicular to the optic axis.

In this study, the 2D material BA_2PbI_4 exhibits an orthorhombic structure (space group: Pbca) with lattice parameters a = 8.876 Å, b = 8.693 Å, and c = 27.616 Å, showing pronounced anisotropy along the c-axis. As a result, the real space vector [u v w] can deviate significantly from the reciprocal vector (h k l), which defines the plane normal. For example, **Supplementary Figure S24** shows that the [111] vector and the (111) plane normal differ by 53.1°, while the [101] vector and the (101) plane normal—identical to (202) plane normal—differ by 54.4° in the BA_2PbI_4 unit cell. Hence, diffraction patterns along zone axes [111] or [101] do not imply that the (111) or (101) planes are perpendicular to the optic axis.

To determine real space vectors (zone axes) corresponding to the plane normals of (111) and (101), the reciprocal vector (h k l) is expressed in terms of real space unit vectors.

$$for\ real\ space\ unit\ vectors\ \vec{a} = 8.876\,\vec{\imath}\,, \vec{b} = 8.693\,\vec{\jmath}\,, \vec{c} = 27.616\,\vec{k}$$

$$,where\ \vec{\imath}\,, j\ and\ \vec{k}\ \ are\ cartesian\ unit\ vectors$$

$$(h\ k\ l) = h\frac{\vec{b}\times\vec{c}}{\mathrm{V}} + k\frac{\vec{c}\times\vec{a}}{\mathrm{V}} + l\frac{\vec{a}\times\vec{b}}{\mathrm{V}}$$

$$= h\frac{1}{|\vec{a}|}\,\vec{\imath} + k\frac{1}{|\vec{b}|}\,\vec{\jmath} + l\frac{1}{|\vec{c}|}\,\vec{k}$$

$$= h\frac{1}{|\vec{a}|^2}\,\vec{a} + k\frac{1}{|b|^2}\,\vec{b} + l\frac{1}{|c|^2}\,\vec{c}$$

$$= [\frac{h}{8.876^2}\ \ \frac{k}{8.693^2}\ \ \frac{l}{27.616^2}]$$

Using the lattice parameters, the normals for (111) and (101) are approximately [0.0127, 0.0132, 0.0013] and [0.0127, 0, 0.0013], respectively. However, experimentally identifying these high-index diffraction patterns is challenging due to their sensitivity to sample thickness. **Supplementary Figure S25** presents simulated diffraction patterns for zone axes [9.7, 10.1, 1.0] and [9.7, 0, 1.0], generated using the Single Crystal code for kinematical simulations. These show that peak intensities vary significantly with thickness, hindering reliable zone axis determination. Thus, alternative zone axes less sensitive to thickness variations were sought.

Local regions with diffraction patterns indexed to zone axes [551] and [100], close to [9.7, 10.1, 1.0] and [9.7, 0, 1.0], respectively, were identified. Their angular deviations are 11.3° and 17.3°, respectively, as shown in atomic models in **Supplementary Figure S23**. Experimental patterns were compared to simulations using dynamical convergent beam electron diffraction (convergence angle: 0.3 mrad) via the py4DSTEM code, mimicking nano-beam diffraction conditions. This confirms the presence of localized crystallites with (111) and (101) planes nearly aligned along the optic axis.

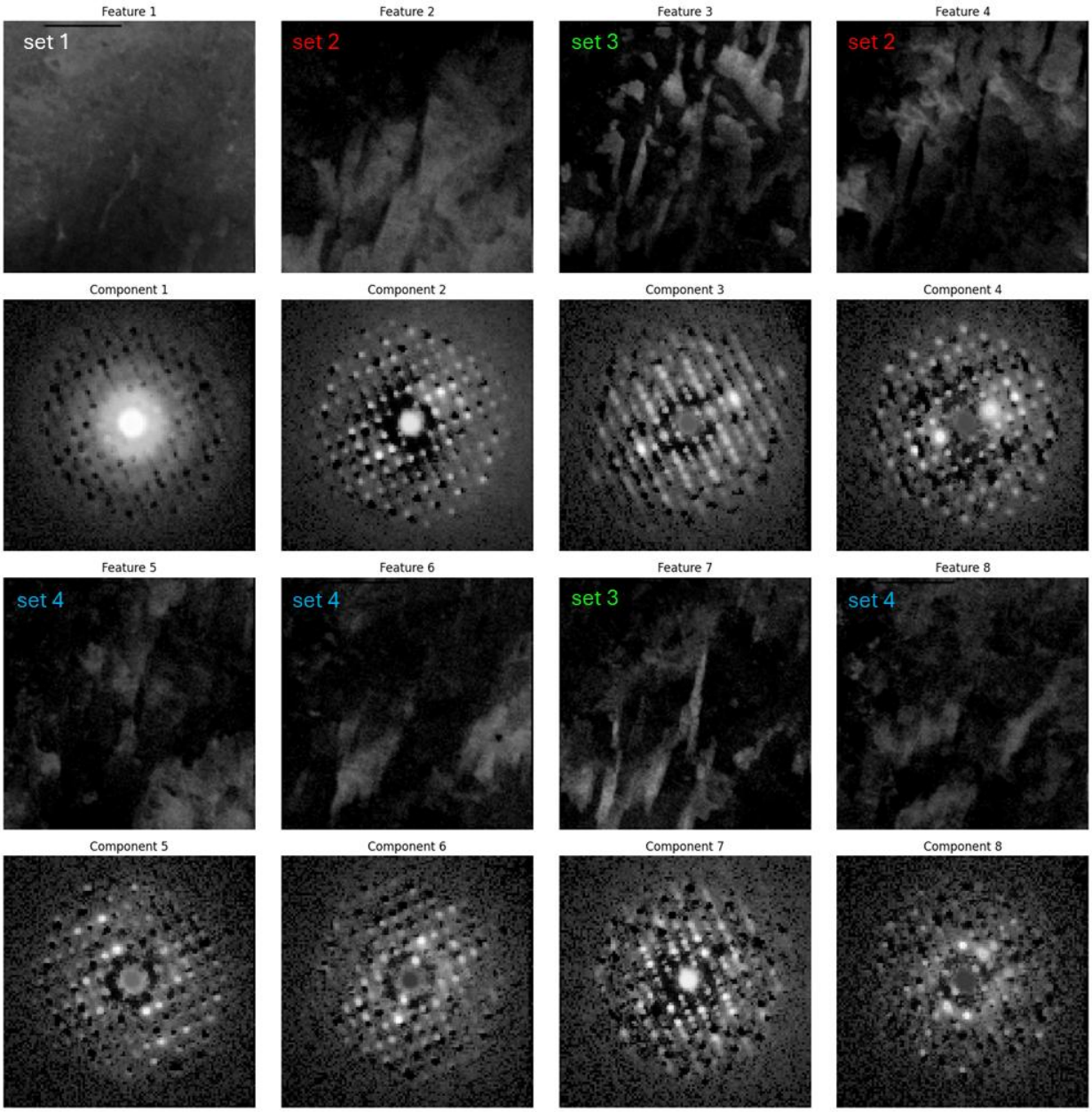

Supplementary Figure S23. Decomposed diffraction patterns from 4D-STEM data of the SICC BA_2PbI_4 film. Dimensionality reduction was performed using non-negative matrix factorization (NMF), resulting in eight features and their corresponding diffraction components. These are classified into four sets: Set 1 represents background intensity, Set 2 primarily shows the [001] zone axis pattern, Set 3 primarily shows the [010] zone axis pattern, and Set 4 is a mixture of all other components.

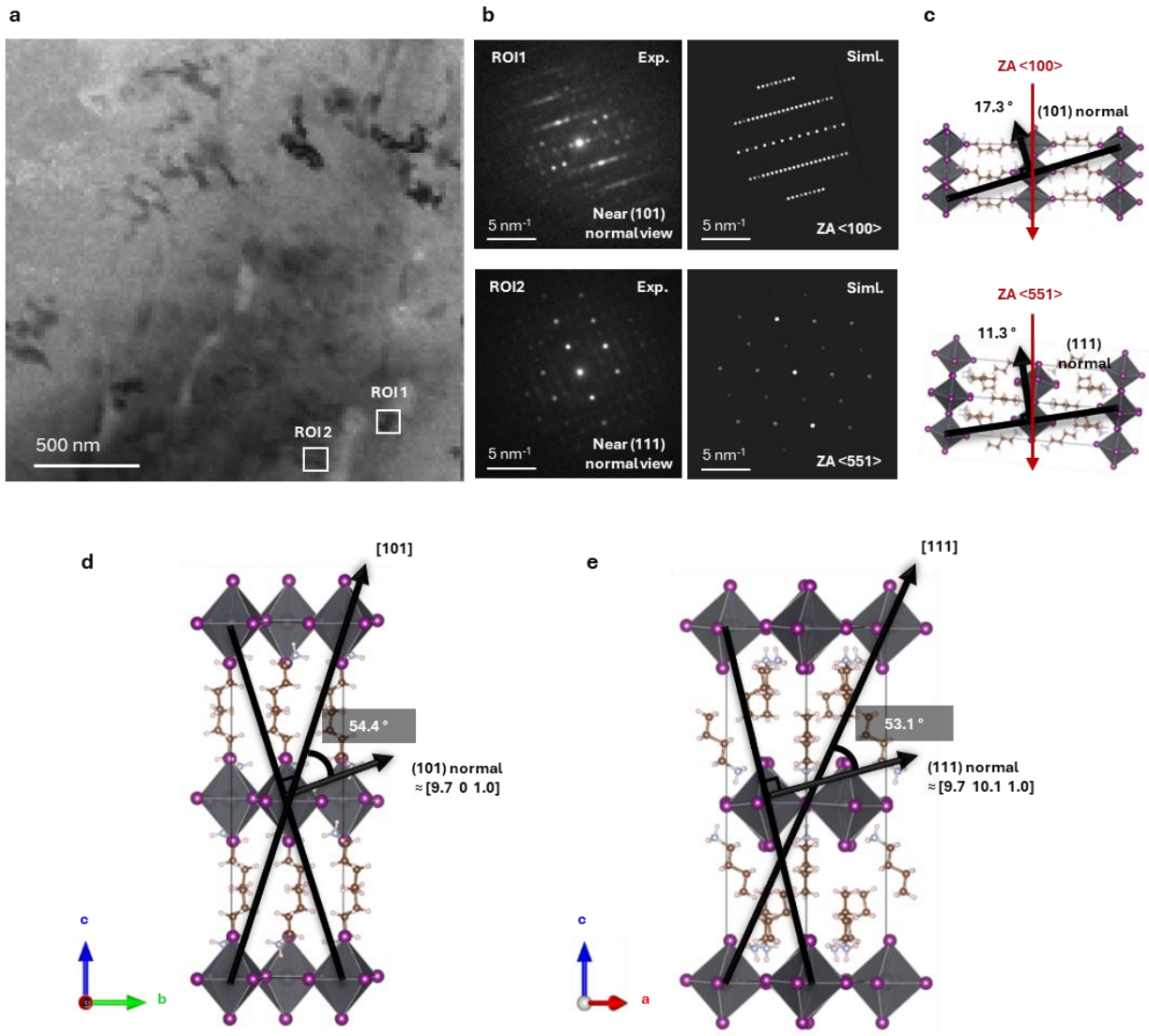

Supplementary Figure S24. Determination of Zone axis(ZA). (a) Virtual-bright field (v-BF) image of the SICC BA_2PbI_4 film. (b) Diffraction patterns obtained from regions of interest (ROI 1 and ROI 2) in (a), along with corresponding simulated diffraction patterns and atomic models, indexed as zone axes (ZA) <100> and <551>, respectively. The simulations were performed using the *py4DSTEM* code based on dynamical convergent beam electron diffraction with a convergence angle of 0.3 mrad. (c) Atomic model showing the [110] direction and the plane normal to the (101) plane, with an angular deviation of 54.4°. (d) Atomic model showing the [111] direction and the plane normal to the (111) plane, with an angular deviation of 53.1°.

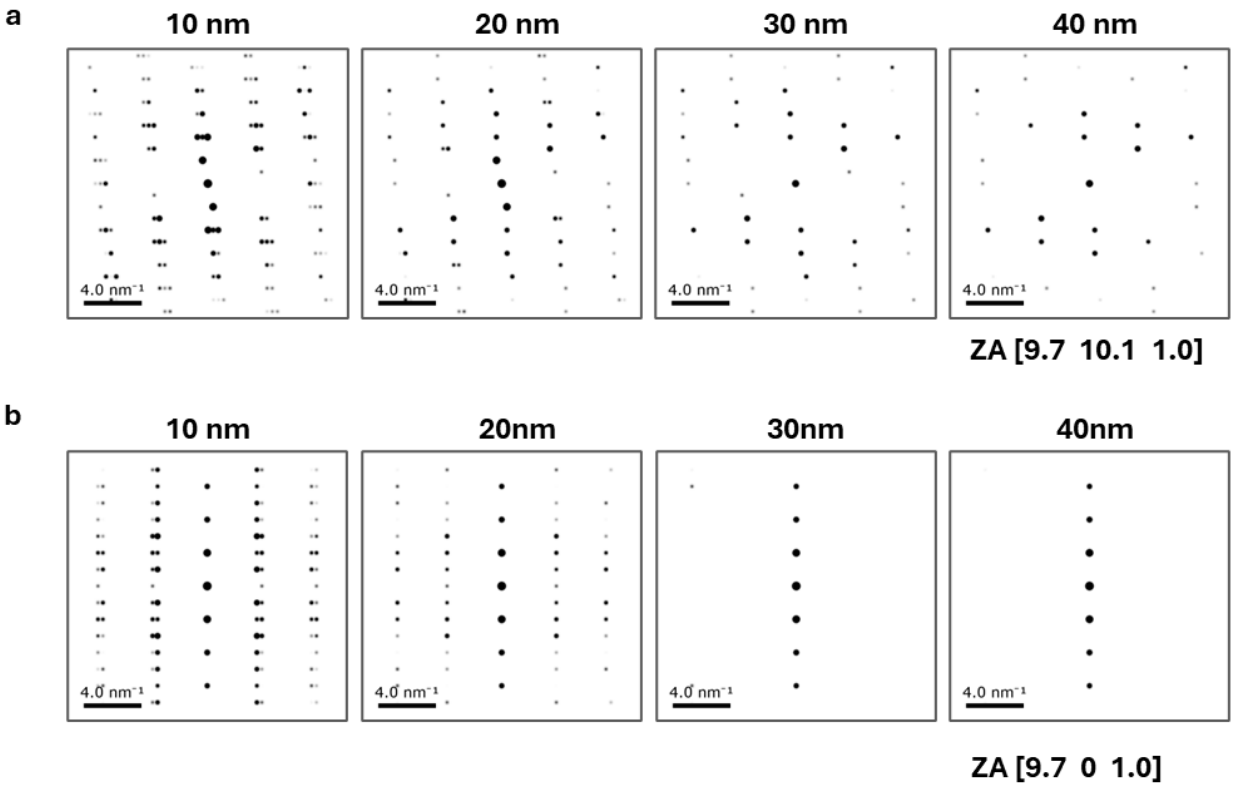

Supplementary Figure S25. Thickness series of simulated diffraction patterns of BA_2PbI_4 from zone axis (a) [9.7 10.1 1.0] and (b) [9.7 0 1.0], respectively. Kinematical calculations were conducted using Single Crystal Code.

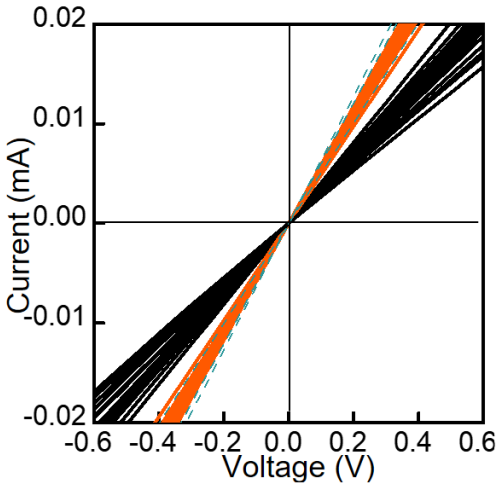

Supplementary Figure S26. IV results of dot devices (ITO/BA_2PbI_4/Au). The orange lines are results of SICC BA_2PbI_4 based dot devices and black lines are results of control BA_2PbI_4 based dot devices. The calculated average of the SICC (5.07E-06 S/cm) and control (1.82E-06 S/cm) were extracted from top 20 dot devices. Abnormal values of control device suggesting carrier transport through Au were observed due to non-uniform regions and were excluded when calculating the average (green dotted line).

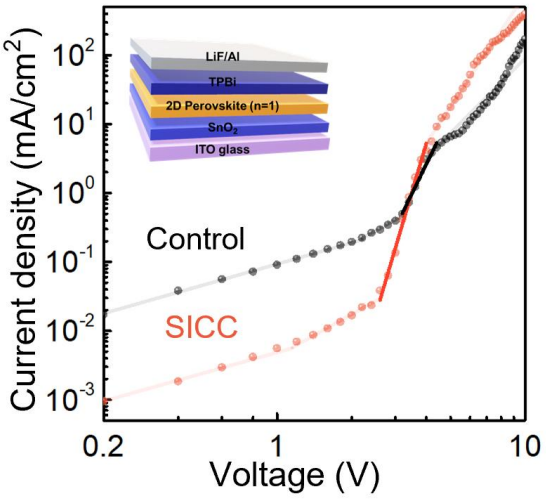

Supplementary Figure S27. The results of Dark current-voltage curve. I-V trace of BA_2PbI_4 film with SICC and control process exhibiting three different regions with $I \propto Vn$ (n=~1; Ohmic, n>3; trap-filled, n=~2; Child). Fitting lines were extracted by using space charge limited current (SCLC) model. The inset figure shows device structure and solid line indicates trap-filled region.

Supplementary Note 3. Calculation of carrier mobility and electronic trap density using the SCLC measurement.

The SCLC measurement was conducted to determine mobility and trap density using an electron-only device structure of ITO/SnO_2/perovskite/TPBi/LiF/Al. The dark current density-voltage (J-V) characteristics of the electron-only devices were measured using a Keithley 2400 sourcemeter at a scan rate of 100 ms and a voltage range from -10 V to 10 V.

The regions were distinguished from the J-V using a log-log scale: (a) ohmic region ($n \approx 1$),(b) Trap-limited SCLC region ($n \approx 2$) (c) Trap-filled SCLC region ($n \geq 3$) (d) Child region (trap-free SCLC, $n \approx 2$), characterized by $J \propto V^n$[39,40]. Additionally, it can be used in three segments excluding Trap-limited SCLC region[41].

The electron mobility then extracts from the child region with Mott−Gurney equation of

$$J = \frac{9}{8}\varepsilon\varepsilon_0\mu\frac{V}{L} \qquad \text{[Equation 3]}$$

Where J is the current density, V are the applied voltage, respectively, ε is the dielectric constant, ε_0 is vacuum permittivity, L is the thickness, and μ is the carrier mobility 1-2.[7,8] Based on this equation, the electron mobility for SICC ($1.7*10^{-1}cm^2V^{-1}s^{-1}$) and control ($3.1*10^{-2}cm^2V^{-1}s^{-1}$) was extracted.

A rapid nonlinear rise in trap-filled limit (TFL) was observed, indicating that all available defect states were filled by the injected carriers. The onset voltage, V_{TFL}, was found to be linearly proportional to the density of defect states:

$$V_{TFL} = \frac{qn_tL^2}{L^3} \qquad \text{[Equation 4]}$$

Where q is the elementary charge and n_t is the trap density. Although the exact point on the J-V curve to be chosen as V_{TFL} has not been clarified, it is typically derived from the intersecting point between the tangent of the ohmic region with $n \approx 1$ and the tangent of the trap filled SCLC region with $n \geq 3$ in most research.[6-9] However, our results revealed four distinct regions in the SCLC. Thus, we identified the trap-limited SCLC region with $n \approx 2$ and the tangent of the trap-filled SCLC region with $n \geq 3$. [4,5] Based on this method, V_{TFL} for SICC (2.61 V) and control (3.21 V) were determined respectively, and by applying them to Equation (4), n_t for SICC ($8.70*10^{15}$ cm^{-3}) and control ($2.41*10^{16}$ cm^{-3}) was extracted, respectively.

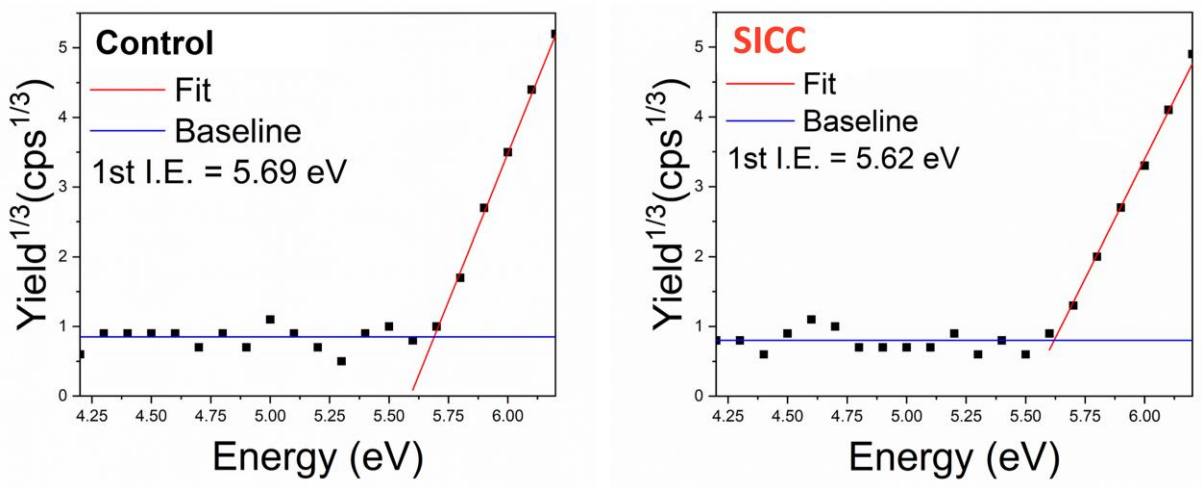

Supplementary Figure S28. Photoemission Yield Spectroscopy in Air (PYSA) measurement results of films. The valence band maximum was calculated as 5.69 eV (with an error of 0.01 eV) in the control sample and 5.62 eV (with an error of 0.01eV) in the SICC sample.

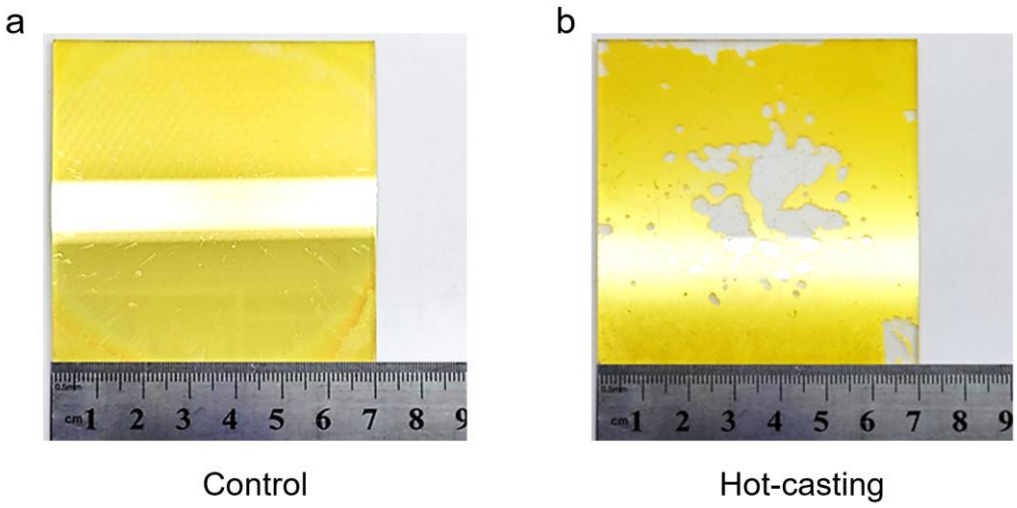

Supplementary Figure S29. The Photographs of BA_2PbI_4 2D perovskite film fabricated on 7 cm x 7 cm glass substrate for (a) control process and (b) Hot-casting method.

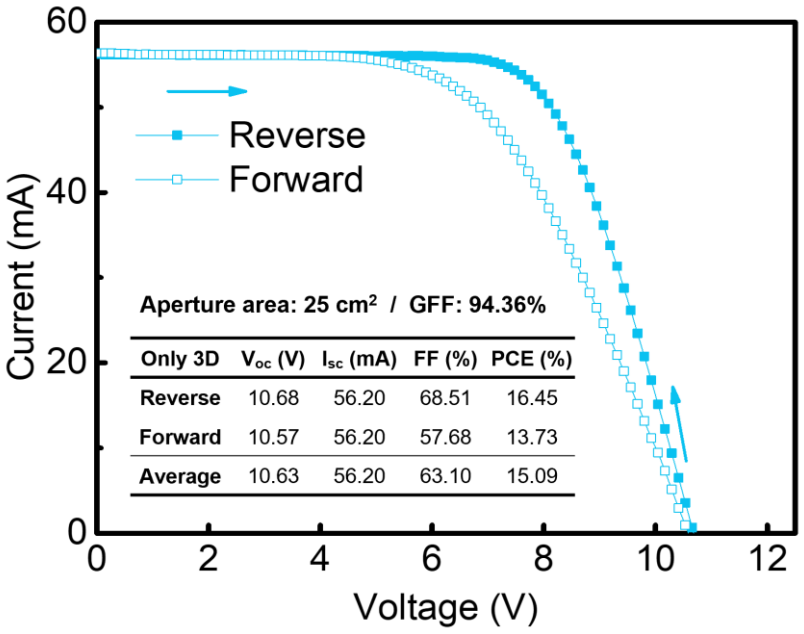

Supplementary Figure S30. I−V curve of the 3D perovskite only solar module. The size of module is 50 cm^2 and the aperture area is 25 cm^2 and the geometry fill factor is 94.36 %. Light blue filled boxes and unfilled boxes indicate the reverse and forward scans, respectively.